Non-Interceptive Beam Current and Position Monitors for a Cyclotron Based Proton Therapy Facility

Srinivasan, Sudharsan

DOI:
10.33612/diss.149817352

Chapter 3: Prototype Tests of the Proton Beam Current Monitor (BCM)

This Chapter is summarized in the following paper:

Sudharsan Srinivasan, Pierre-André Duperrex, Jacobus Maarten Schippers, Beamline characterization of a dielectric-filled reentrant cavity resonator as beam current monitor for a medical cyclotron facility, Physica Medica, Volume 78 ,2020, Pages 101-108, ISSN 1120-1797. Doi: https://doi.org/10.1016/j.ejmp.2020.09.006.

3.1 Introduction

In the previous Chapter, we characterized the cavity resonator with the help of HFSS Eigenmode and Driven modal solvers. The simulation results of the cavity resonator provided an estimate of the signal level that we could expect in beam current measurements. Moreover, the simulation provides properties of the cavity, which include mutual pickup coupling and the loaded quality factor. These serve as the foundation to validate the cavity in the real-world before beamline installation.

In this Chapter, the test-bench characterization of the cavity is described. The results of the test-bench characterization are compared with the simulation results, which provides confidence in the signal estimate and the properties of the cavity. Also discussed in this Chapter are the beamline measurements of the cavity resonator for proton beam energies in the range 238-70 MeV for the beam current in the range 0.1-10 nA.

3.2 Purpose of a test-bench

For any beam diagnostic element, before its installation in the beamline, it is important to characterize it as a stand-alone device in the lab. For this purpose, a test-bench environment has been developed, similar to the simulation world. The main function of the test-bench is to perform network analysis of the cavity resonator (Device Under Test (DUT)) as a multiport device. The network analysis measurements of the DUT provide the resonance frequency and its 3 dB bandwidth, which provides information on the loaded quality factor Q_L. In addition, the mutual pickup coupling coefficients and the beam-pickup coupling

coefficients are derived from the S-parameter (Scattering) measurements. These measurements serve as the basis for the validation and characterization of the prototype. The test-bench characterization is performed in two stages of the S-parameter measurement similar to the simulation:

- Without a beam analog, to measure cavity properties such as mutual pickup coupling as $S-$parameters, and loaded Q (to validate the prototype). The mutual pickup coupling provides information on the loaded quality factor of the stand-alone cavity. The external quality factor is derived from the loaded quality factor measurement (Chapter 2).
- With a beam analogon, to measure the S-parameters between the beam entrance port and a large pickup port (to measure the pickup signal). These S-parameters help to determine the pickup signal in units of voltage as a function of beam current.

3.3 Stand-alone test-bench and its components

The fundamental design concept for the test-bench is a vertical mounting of the BCM prototype along with its main stand elements. The main stand elements include two reference boxes on either end of the beam pipe extensions. We prefer such a design as it is easy to accommodate different prototypes (also for BPM later in Chapter 5). This design aids in realizing a beam analog, i.e., a stretched wire passing through the hollow center of the prototype. In this way, wire bending due to gravity is prevented and orthogonality to the cross-sectional plane of the prototype is maintained. Figure 3.1 represents the design sketch of the test-bench with DUT and the lab environment of the same setup. The description of the test-bench elements is provided in the following subsection.

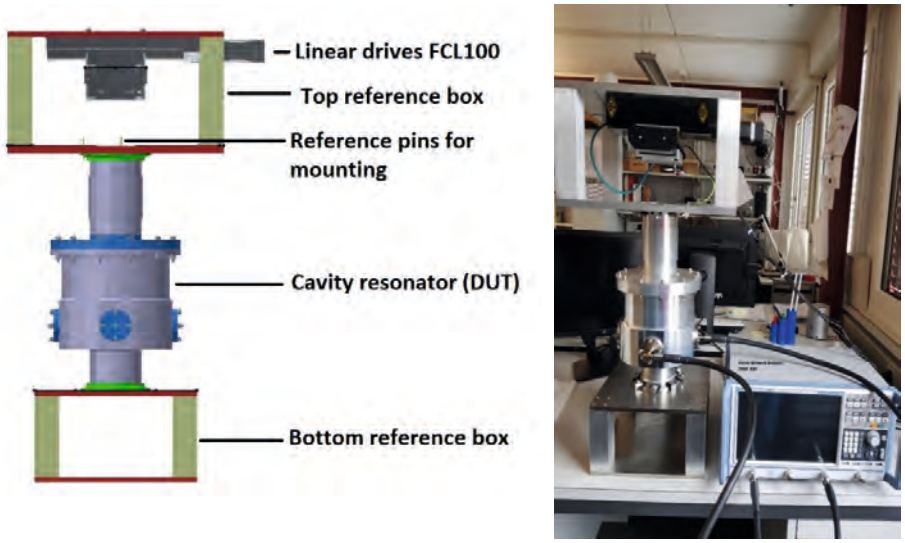

Figure 3.1: Design sketch and lab environment of the stand-alone test-bench. In the lab environment, ZNB8, a network analyzer from Rohde and Schwarz is used to make S-parameter measurements. FCL100 series linear drives move the stretched wire. The cavity characterization is performed to determine mutual pickup coupling, loaded quality factor and the beam-pickup coupling between the stretched wire and a large pickup.

3.3.1 Beam Current Monitor and its assembly components

The BCM is the DUT that we characterize on the test-bench. We designed the prototype (design parameters discussed in Chapter 2) with beam tubes with an inner diameter of 90 mm (standard PROSCAN beam pipe dimension) as pipe extension and four measurement ports (two large pickup loops and two small pickup loops). The purpose of having four measurement ports is discussed in Chapter 2 (subsection 2.4.3). The prototype is attached with non-rotatable flanges on either side for easy installation on the test-bench.

The test-bench consists of two reference boxes (top and bottom) sandwiching the prototype in-between. The linear drives are mounted in XY configuration inside the top reference box, as shown in Figure 3.1. The linear drives are used to position the stretched wire at multiple positions in order to measure the position dependence of the beam current monitor response and later for test-bench characterization of the beam position monitor (BPM) discussed in Chapter 5. The linear drive is a motorized precision stage with a maximum travel range of 100 mm on an integrated stepper motor/controller [1] with a guaranteed on-axis position accuracy and bi-directional repeatability of ± 2.5 µm.

3.3.2 Beam analog

A copper wire of 0.2 mm diameter serves as a beam analogon for the estimation of pickup signals for a given beam current. This is equivalent to the beam analogon used in the HFSS simulation. The copper wire is suspended with a hanging weight in an oil well. The stretched wire setup replicates a coaxial line equivalent to the simulation setup performed in Chapter 2. Since network analyzers have a source impedance of 50 Ω, a resistor of 316 Ω is connected in series to the beam analogon at the excitation port to match the characteristic impedance of the coax line consisting of the beam pipe and the stretched wire. This minimizes reflections and provides undisturbed excitation signals as shown in subsection 3.4.3. The influence of reflection on the beam analogon is considered negligible anyway since the length of the stretched wire is small compared to the wavelength of the resonance frequency. To verify the position independence of the monopole mode of the beam current monitor, S_{ji} (j is the pickup port and i is the beam entrance port) measurements are performed at the center position (0, 0) and at an offset position (20, 20).

The BCM characterization, both with and without beam analog, is performed with a ZNB8 vector network analyzer [2]. Calibration techniques and the network analyzer functioning are described briefly in the Appendix. More detailed information can be found in [3].

NOTE: *The structural analysis of the test-bench with the prototype was performed with the Autodesk Inventor suite [4]. The test-bench is a safe platform that does not induce mechanical deformation that could shift the resonance frequency.*

3.4 S-parameter measurements

S-parameters are used as the reference to characterize the beam current monitor [5]. The S-parameters measured with a vector network analyzer are fundamentally the complex ratio of wave quantities while exciting the DUT with a stimulus at its various ports. In the previous Chapter, we mentioned the transmission S_{ji} as the ratio of output power (port *j*) to input power (port *i*) and as a means to measure mutual pickup coupling coefficients and to measure pickup signal sensitivity. Since for both measurement scenarios, the S_{ji} transmission is measured as a two-port measurement; the representation of the S-parameters for a two-port model is shown in Figure 3.2.

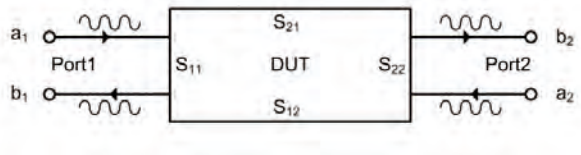

Figure 3.2: Two-port S-parameter model

Each port has a transmission index represented as ‘a’ and a reflective index represented as ‘b’. For example, S_{21} is the transmission coefficient for a wave with port 1 as a source and port 2 as a receiver such that $S_{21}=b_2/a_1$. Similarly, S_{11} is the reflection coefficient at port 1 given by $S_{11}=b_1/a_1$. For the characterization of the prototype, we consider the transmission coefficients for comparison with simulation results. Moreover, it is important that we terminate the ports of the DUT not in use with a 50 Ω termination, as we simulated the prototype with such boundary conditions, as mentioned in Chapter 2. In the following, the mutual pickup transmission coefficients and the optimization of the resonance frequency will be discussed, followed by the results of the transmission coefficient measurement between the beam analogon and the pickups.

3.4.1 Mutual pickup S-transmission (S_{ji}) results

The mutual pickup S-transmission coefficient measurements are performed in the absence of the beam analogon. In this subsection, the measured mutual pickup coupling between a large (j=3) and a small pickup (i=4) is shown in Figure 3.4. The measurement and simulation results of the S_{ji} coefficients for all possible pickup combinations are summarized in Table 3.1. Also included are the resonance frequency, and the loaded quality factor, Q_L. We represent an example measurement scheme, S_{34}, in Figure 3.3.

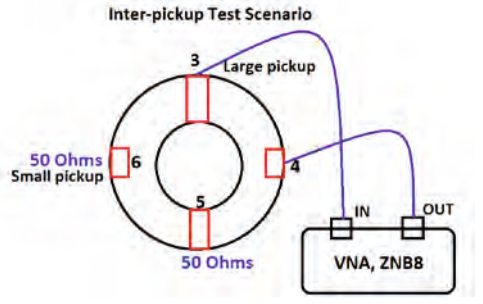

Figure 3.3: Mutual pickup coupling measurement setup between a large (nr 3 and 5) and a small (nr 4 and 6) pickup in the absence of a stretched wire (which would have nrs 1 and 2). These measurements provide information on the loaded quality factor and the resonance frequency of the beam current monitor as a stand-alone DUT.

Table 3.1: Measured S_{ji} transmission parameters for all possible mutual pickup combinations. Included are the TM_{010} resonance frequency, peak coefficient, and loaded quality factor. The resonance frequency from the simulation is provided for comparison.

S-Parameter	Simulated Resonance Frequency (MHz)	Measured Resonance Frequency (MHz)	Simulated S-Peak (dB)	Measured S-Peak (dB)	Simulated Q-Factor	Measured Q-Factor
S-34	145.7	148.64	−23.38	−21.88	40.58	40.87
S-35	145.7	148.68	−1.53	−1.34	40.58	40.77
S-36	145.7	148.64	−23.38	−21.22	40.58	40.75
S-45	145.7	148.64	−23.38	−21.89	40.58	40.58
S-46	145.7	148.69	−45.22	−41.78	40.58	40.73
S-56	145.7	148.64	−23.38	−21.23	40.58	40.64

From the above results, the observations could be summarized as:

- The average of the measured resonance frequency (i.e., 148.65 MHz) is 2 % higher than the design resonance frequency of 145.7 MHz.
- The measured S_{ji} is higher than the simulated S_{ji} for all mutual pickup combinations.
- The measured loaded quality factor of the prototype is in good agreement with the simulation.
- The coupling between two large pickup loops (S_{35}) corresponds in voltage ratio is $V_{out}/V_{in} \approx 0.85$. The coupling between two small pickup loops (S_{46}) is $V_{out}/V_{in} \approx 0.0081$. The coupling between a large and a small pickup loop ($S_{34, 36, 45, 56}$) is $V_{out}/V_{in} \approx 0.081$.

Comparing the transmission coefficients of S_{34} vs S_{46}, we can deduce that the sensitivity of the large pickup is approximately factor 10 higher than the small pickup. This agrees with the ratio of the area between the large pickup loop (1172 mm^2) and the small pickup loop (114 mm^2).
The measured coupling coefficients, especially between two small pickups (S_{46}) or between a small pickup and a large pickup (such as $S_{34, 36, 45, 56}$) is minimum 2 dB higher than the simulation. Some construction issues that we cannot exclude might have contributed to these differences. Nevertheless, the mutual pickup coupling of the two large pickups (S_{35}) is in good agreement with the simulation (see S_{34} between simulation and measured in Table 3.1) and as these loops are used to measure the beam-pickup coupling, the differences in mutual pickup coupling for $S_{34, 36, 45, 56, 46}$ are not of major concern.

The only deviation of concern is the resonance frequency with respect to the simulation, which is optimized (i.e., tuned) as shown in the next subsection.

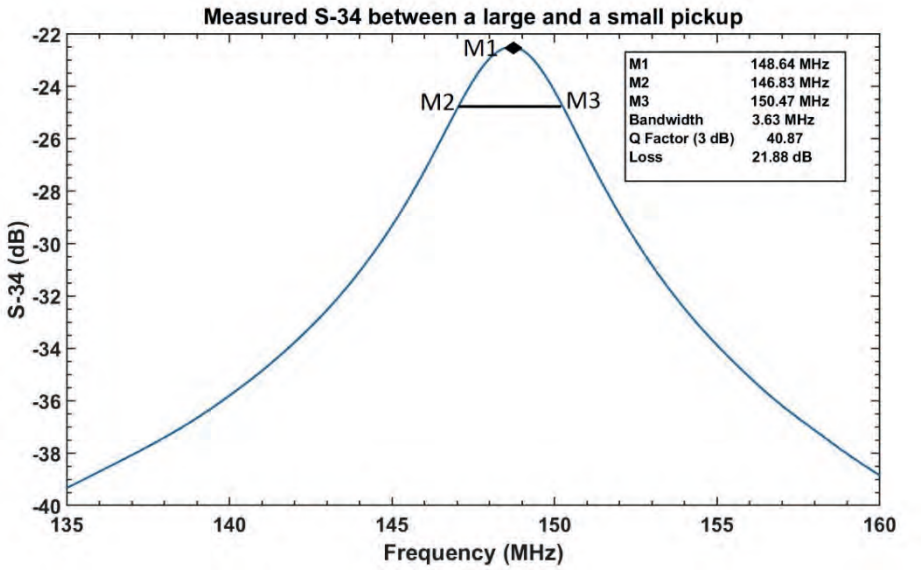

Figure 3.4: Measured S-34, transmission coefficient between a large and a small pickup of the prototype.

3.4.2 Resonance frequency optimization

The source of error for the difference in the resonance frequency is the difference in the dielectric constant of the macor. The equivalent dielectric constant is estimated as 5.7 at approximately 150 MHz compared to 6.0, which was used to determine the ring dimensions. This constitutes to 5% decrease in the equivalent capacitance, which results in approximately 2% (square root) increase in the resonance frequency i.e., 148.64 MHz as observed. This difference could be due to the frequency dependence of the dielectric constant [6], in combination with a different dielectric constant of the material supplied.

HFSS simulation results as shown in Figure 3.5 confirms the above assumption of the 2% increase in the resonance frequency. As seen in Chapter 2, the resonance frequency can be optimized by varying the dimensions of the dielectric. Since the prototype is already manufactured, the resonance frequency can be tuned only by changing the dielectric width. From parametric analysis studies, a dielectric width of the optimized macor ring of **33 mm** is chosen as the optimal macor width dimension. The beam current monitor with the modified macor ring is used to characterize the pickup sensitivity in the presence of a beam analog, as described below.

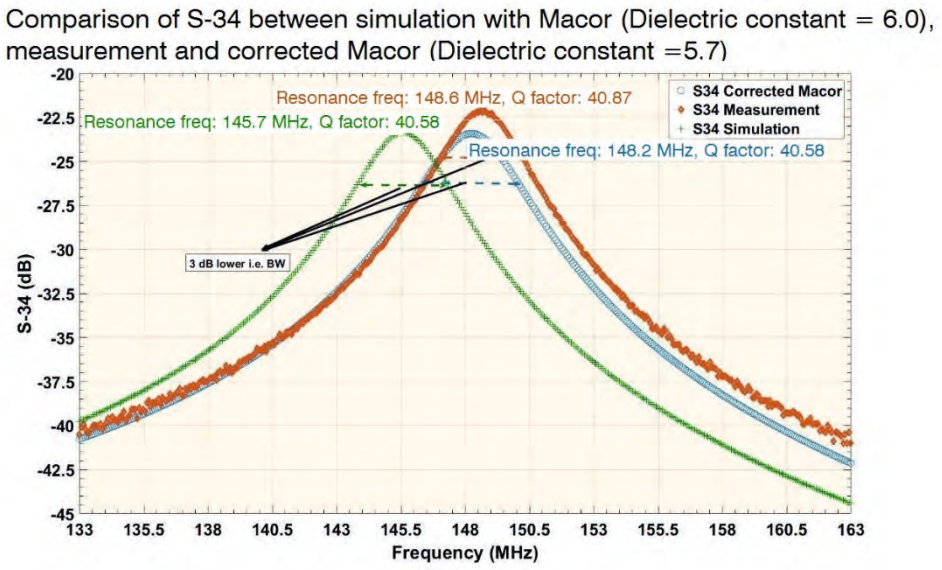

Figure 3.5: Updated S-34 plot of the beam current monitor with a dielectric constant of 5.7.

3.4.3 Beam-Pickup S-transmission parameter

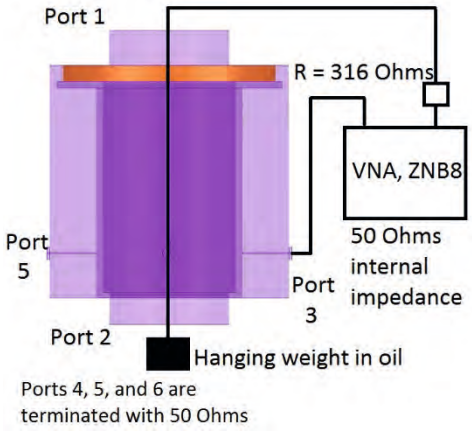

Figure 3.6: Test Scenario for Beam-pickup S-transmission measurement. The Vector Network Analyzer (VNA) provides a source signal at 145.7 MHz with a span of 30 MHz (130.0 MHz-160.0 MHz).

We performed an S-transmission coefficient measurement between the stretched wire (beam analogon) and one of the large pickups. This provides the pickup sensitivity for a given beam current transiting through the stretched wire, which is compared with the simulation results. Since the stretched wire forms a coaxial

line with the DUT, to minimize reflections, impedance matching is implemented. The impedance is matched only at port 1, as shown in Figure 3.6, as the other end of the stretched wire is suspended in an oil well with a hanging weight. As discussed in subsection 3.3.2, the impedance matching at port 1 is achieved by placing an ohmic resistor of 316 Ω to match (to 366 Ω characteristic impedance). For the beam-pickup measurement, the voltage ratio is not used since the two ports are not terminated with the same impedance values. Hence, the power ratio is used to determine beam-pickup coupling from S_{31} measurements. For a pickup port terminated with 50 Ω, we can expect the pickup voltage in the range as given in Chapter 2.

S_{31} is measured at two different beam positions similar to the simulation: at (0,0), the center position and at (20,20), a position that corresponds to 60% of the beam pipe radius as shown in Figure 3.7. The measured resonance frequency is 145.7 MHz. It is important to see the good agreements between measurement and simulation after replacing the macor. The position dependence of the cavity resonator sensitivity is approximately 0.03%/mm up to 60% of the beam pipe radius. This is because the Bessel function of the order m = 0 is nearly independent of the radius close to the cavity center [7].

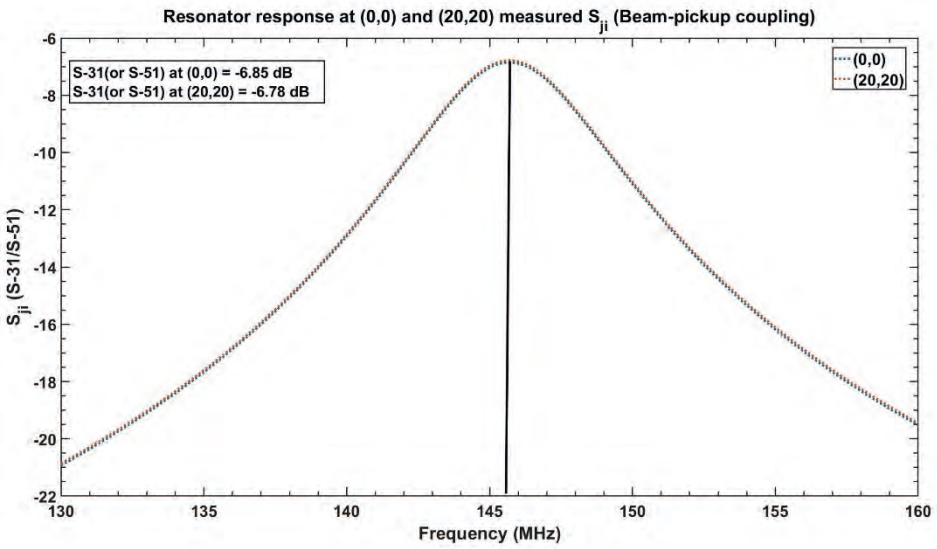

Figure 3.7: S31 measured at (0,0) and at (20,20) in the test-bench, confirming the position independency of the resonator.

The measurements confirm that for a beam current of 1nA at 72.85 MHz, we can expect the pickup signal to be at approximately 15 nV (rms) and the

corresponding power is -143 dBm. To read such low signals into the measurement system, we need high-gain low-noise amplifiers and high-resolution Analog-to-Digital Converters (ADCs). It is important to consider the losses (≈4 dB) associated with long measurement cables, connectors, ADCs and amplifiers in the operational situation, as in the test-bench measurements and in the simulation, these were not considered. Thus, the thermal noise floor for a 50 Ω is raised to -170 dBm (≈0.7 nV) from -174 dBm for a measurement bandwidth of 1 Hz. For the beam current of 1 nA, we expect the SNR at approximately 27 dB (-143 dBm +170 dBm).

3.5 Beamline characterization

The validation of the prototype has been completed with beamline measurements. For the resonator to deliver the same signal sensitivity independent of the beam energy, the resonator must be located not too far downstream of the degrader. Otherwise, with decreasing proton energy, the bunch length is increased due to the contribution of the degrader to the energy spread in the beam as described in Chapter 1. This will lower the amplitude of the second harmonic component in the bunch, which will reduce the resonator sensitivity at lower proton energies. Thus, to measure the beam current in the energy range 238-70 MeV with an energy independent sensitivity, the resonator should be located close to the degrader exit in the ideal case. However, this may not be the location where the beam current has to be or can be measured. The effect of the distance between the resonator and the degrader on the sensitivity of the resonator is described in the following subsection.

3.5.1 BCM location in the PROSCAN layout and the effect of bunch length

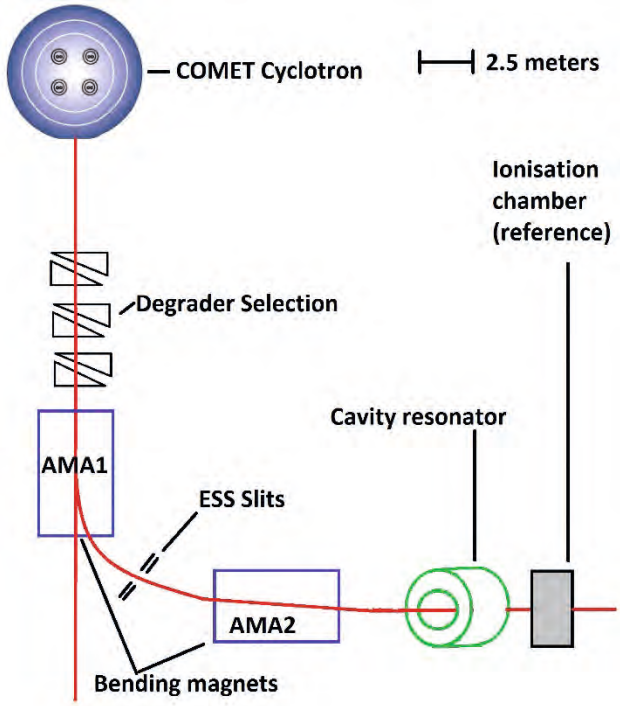

Figure 3.8: PROSCAN beamline layout with the beam current monitor location highlighted.

The PROSCAN facility is temperature-controlled (28.5 ± 0.5 °C), in order to have stable operating conditions for its beamline elements. In PROSCAN, delivery of multiple beam energies in the range 238-70 MeV is achieved by means of a carbon wedge degrader [8]. The degradation of the beam energy results in the growth of the emittance and energy spread [9]–[11]. To have the required beam quality at the patient location, the beam is shaped by a set of collimators and an Energy Selection System (ESS) that helps in controlling the energy spread at the patient location. An emittance of $30\,\pi$ mm mrad and a maximum momentum spread of ±1.0% is allowed to match the acceptance (emittance and momentum) of beamlines and gantries [8]. The increase of the energy spread leads to an energy-dependent decrease in bunch amplitude and an increase in bunch length down the beamline in the beam current. Thus at 16 meters from the degrader where the cavity resonator is positioned as marked in Figure 3.8, the second harmonic of the beam repetition rate is reduced because of this effect.

For beamline validation of the cavity resonator, multiple energies are chosen as given in Table 3.2. The energy spread induced by the degrader at these energies is calculated as per [12] and is within an acceptable range of the measured energy spread as given in [13]. For energies lower than 180 MeV, the ESS helps in reducing the momentum spread to ±1%, but at the energies 231 MeV and 201 MeV, the momentum spread is smaller than 1% and therefore not limited by the ESS.

The bunch length at the location of the resonator is estimated from the momentum spread for different energies. Due to the momentum selection in the ESS, a rectangular distribution can be assumed for the shape of the beam bunches. Therefore we have assumed that the harmonic amplitude factor for the second harmonic is only affected by the lengthening of the bunches and not by a shape change [14]. The estimate of the second harmonic amplitude factor, A_2, which is normalized to the average beam current, decreases with increasing bunch length as given in Table 3.2.

Table 3.2: Estimate of the second harmonic amplitude factor for a rectangular bunch shape [14] at the resonator location for different beam energies. A bunch length of 2 ns at the degrader exit is assumed as reference for the calculation.

Energy, MeV	Energy Spread, MeV	Momentum spread, %	Bunch length at resonator, ns	2nd Harmonic Amplitude Factor (A_2)
79	4.4	1.0	3.24	0.67
109	4.2	1.0	3.08	0.69
139	3.9	1.0	2.97	0.71
171	3.3	1.0	2.91	0.73
201	2.7	0.84	2.71	0.76
231	1.7	0.70	2.56	0.79

3.5.2 Measurement chain

For the beam current measurements with the cavity resonator, a PSI developed measurement system called VME MESTRA is used [15]. The measurement system is configured to convert the amplitude of the 145.7 MHz RF-signal from the cavity into a proportional voltage signal. The measurement chain, as shown in Figure 3.9, starts with a measurement port, i.e., a large inductive loop of the cavity resonator. The other large inductive loop is connected to a resonance trombone for tuning capabilities. The pair of the small inductive loops are terminated with 50 Ω. The cavity signal is amplified with a low-noise amplifier of 29 dB gain [16]. The amplified signal is then bandpass (BP) filtered (40 dB suppression) with a customized cavity-type filter from KL microwave [17]. The bandpass filter has its center frequency at 145.0 MHz with a 3 dB bandwidth of 8.24 MHz. The filtered signal is further amplified by a 40 dB gain with a FEMTO wideband low-noise amplifier [18]. The filtered and amplified signals from the cavity enter the main sub-system of the measurement system, whose components are:

- 2× 25 dB preamplifier [19]
- 16-bit Digitizer (30μV resolution) (ADC3110) [20] with 50.0 MSamples/s sampling rate, maximum input power 10 dBm (2 $V_{peak\text{-}peak}$)
- Digital Down Converter (DDC)

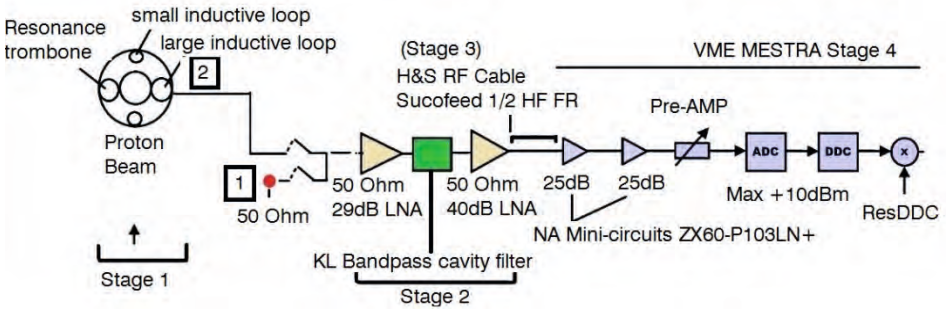

Figure 3.9: Measurement chain representation from the resonator to the electronic cubicle. Two low-noise amplifiers with gains of 35 dB and 40 dB, a passband filter with a center frequency of 145.0 MHz (3 dB bandwidth = 8.24 MHz), Sucofeed RF cables, VME MESTRA are the measurement chain elements. The small inductive loops are terminated with 50 Ω. The switches before Stage 2 indicate the two different measurement scenarios. Scenario 1 represents 50 Ω on the input of the measurement chain represents Stage 2-4. Scenario 2 represents the resonator connected to the measurement chain represents Stage 1-4.

The digitized signal is down-converted through a Field Programmable Gate Array (FPGA) on the Digital Down Converter (DDC). The DDC results in an output signal, Res DDC (in counts), with 50 k samples/s following a reduction with a factor of 1000 of the input signal. The DDC filters the input noise power of the digitized signal with its 18 kHz (3 dB) bandwidth in order to get a high attenuation for the stopband and a flat passband. For a beam current of 1 nA at the resonator location, the power budget of the measurement system, integrated over 1 second, is given in Table 3.3.

Table 3.3: Power budget of the measurement system for 1nA beam current as excitation for the cavity resonator.

Stage	measurement system elements	Gain (dB)	Cumulative power level (dBm)
1	Resonator	-	-143.0
2	Local amplifiers	+69.0	-74.0
3	½" H&S SUCOFEED cable 50 m	-2.0	-76.0
4	VME MESTRA total amplification	+50.0	-26.0

3.6 Measurement results

3.6.1 No-beam response with and without the resonator

Prior to the in-beam characterization of the cavity resonator, the no-beam response is measured without resonator (scenario 1 marked in Figure 3.9) and with the resonator (scenario 2 marked in Figure 3.9) in the measurement chain. This measurement was performed while the cyclotron RF was switched on but with no beam traversing the monitor for both the scenarios.

Without the resonator, the DDC output signal for a 50 Ω termination on the measurement cable (scenario 1, Figure 3.9) was recorded as 40000 counts (noise) with a standard deviation of 1.3%. The measurement offset, which is the no-beam resonator response (scenario 2, Figure 3.9) is recorded as $I_{measoff}$ = 63007 counts with a standard deviation of 1.3% (approximately 800 counts). This is representative of the RF interference of the resonator from the cyclotron and the noise floor of the measurement chain. The difference between the two values is the amplitude of the RF interference in counts.

3.6.2 In-beam resonator response

The resonator response is measured for beam current sweeps in the range 0-2.5 nA for the beam energies given in Table 3.2. For the calibration of the cavity resonator as a beam current monitor, an IC [21], [22] is used as a reference monitor, as marked in Figure 3.8. The reference monitor immediately behind the resonator was used for this in order to have the same beam current amplitude. The measured resonator response with respect to the beam current at

231 MeV is shown in Figure 3.10. The standard deviation of the measured response at every beam current is approximately 800 counts.

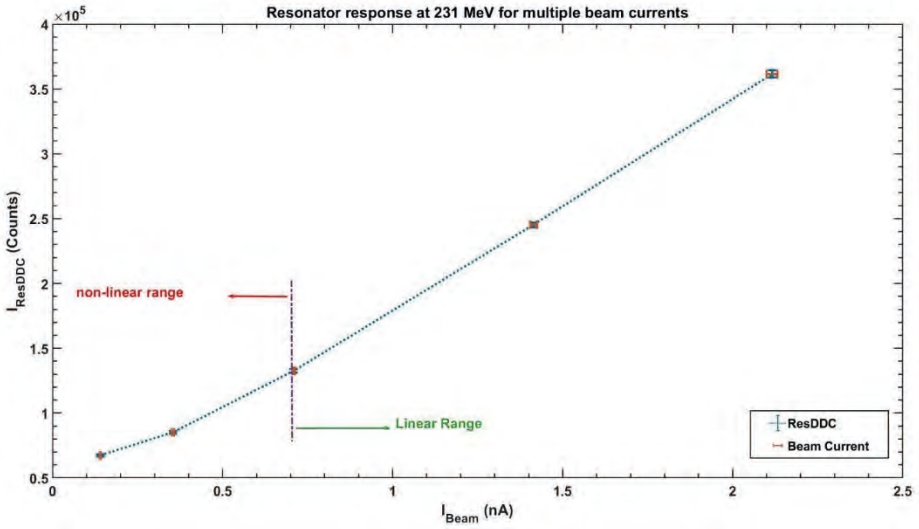

Figure 3.10: Resonator response (ResDDC) in counts at 231 MeV for multiple beam currents. Marked are the non-linear and the linear range of the resonator response with beam current. The dotted line represents the trend of the measurement.

As marked in Figure 3.10, for high beam currents, the relation between the resonator response (given as I_{ResDDC} in counts) and the absolute beam current (given as I_{beam} in nA) can be considered linear after neglecting the measurement offset contributions (smaller effect on the measurement):

$$I_{ResDDC} = kI_{beam} \tag{3.1}$$

where k is the resonator sensitivity whose unit is counts/nA. However, for low beam intensities, as marked in Figure 3.10, the relation between I_{ResDDC} and the I_{beam} is non-linear since the I_{ResDDC} is close to the measurement offset, $I_{measoff}$. For lower beam currents, the relationship can be given by

$$I^2_{ResDDC} = I^2_{measoff} + k^2 I^2_{beam} \tag{3.2}$$

where the power of the measured signal (I^2_{ResDDC}) is the sum of the individual power of the measurement offset ($I^2_{measoff}$) and the power of the beam current response ($k^2 I^2_{beam}$). Such a relation is possible under the consideration that the beam current response and the measurement offset are uncorrelated.

Figure 3.11 represents the beam current measurement represented in power form, i.e., I^2_{ResDDC}, with respect to the power of the beam current, i.e., I^2_{beam}, for all energies. The linear fit is of the form as represented in Eq (3.2) where the intercept term of the linear fit equations is the power of the measurement offset $I^2_{measoff}$ and the slope term is square of the resonator sensitivity, i.e., k^2. The measurement offset and the resonator sensitivity are given as the square root of the intercept term and of the slope term from Figure 3.11 and are summarized in Table 3.4.

The measurement offset derived from the fit intercept term for all energies is within an acceptable range of the no beam resonator response, i.e., 63007 counts. This indicates that there has been no presence of unexpected noise contributions during the measurement. The measured resonator sensitivity, k_meas (in units of counts/nA), given in Table 3.4, decreases with beam energy as expected (i.e., expected resonator sensitivity, k) due to the energy-dependent decrease in the relative amplitude of the second harmonic. This trend is clearly represented in Figure 3.12.

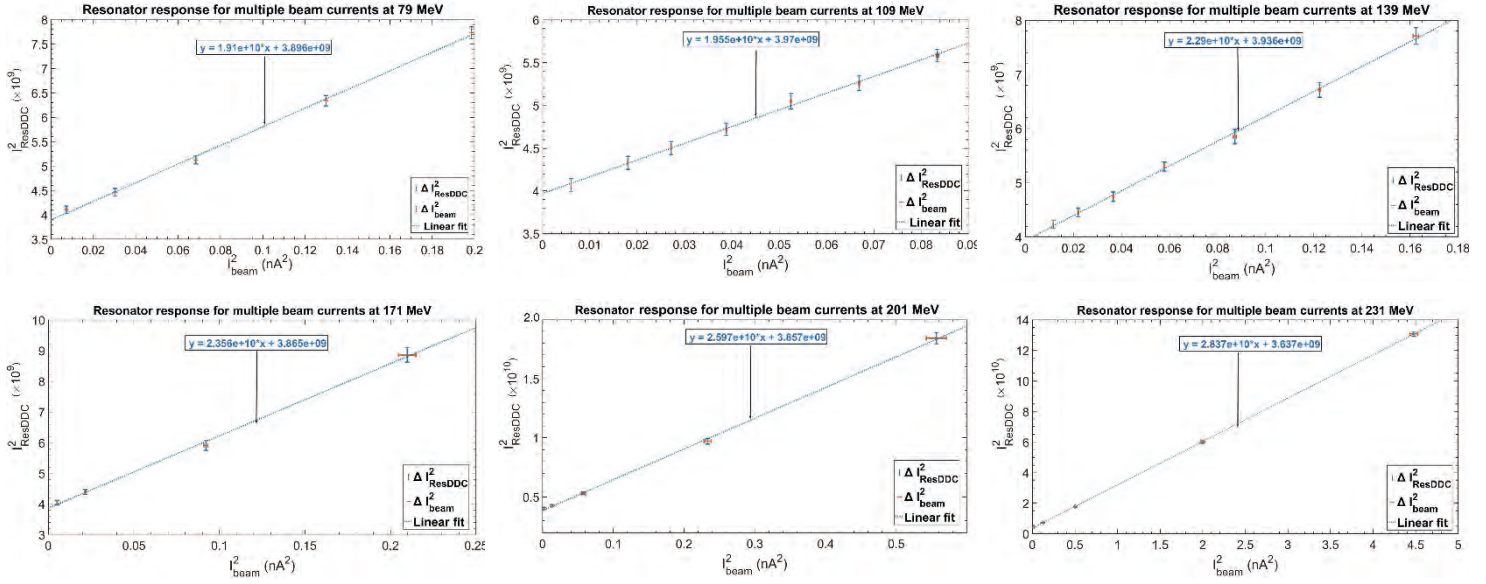

Figure 3.11: Resonator response for beam energies in MeV: 79, 109, 139, 171, 201, and 231 with linear-fit as per represented in dotted lines. The square root of the intercept and of the slope term represent measurement offset in counts and sensitivity in counts/nA. The data points are represented with one sigma deviation. The dotted line represents the linear fit.

Table 3.4: Measurement summary for resonator at different energies. The fractional uncertainty of the evaluated measurement offset and the resonator calibration factor is derived from the in-beam measurements through error propagation. The value of the normalizing term, C=212042 counts/nA. A_2 is taken from Table 3.2.

Proton Beam Energy (MeV)	**Measured Resonator sensitivity, k_meas (±1.35%) (counts/nA)**	**Expected Resonator sensitivity, k (=A_2*C) (counts/nA)**	**Measurement offset, $I_{measoff}$ (±1.26%) (counts)**
79	138202	142068	62418
109	139821	146309	63008
139	151327	150550	62737
171	153493	154791	62169
201	161152	161152	62104
231	168434	167513	60308

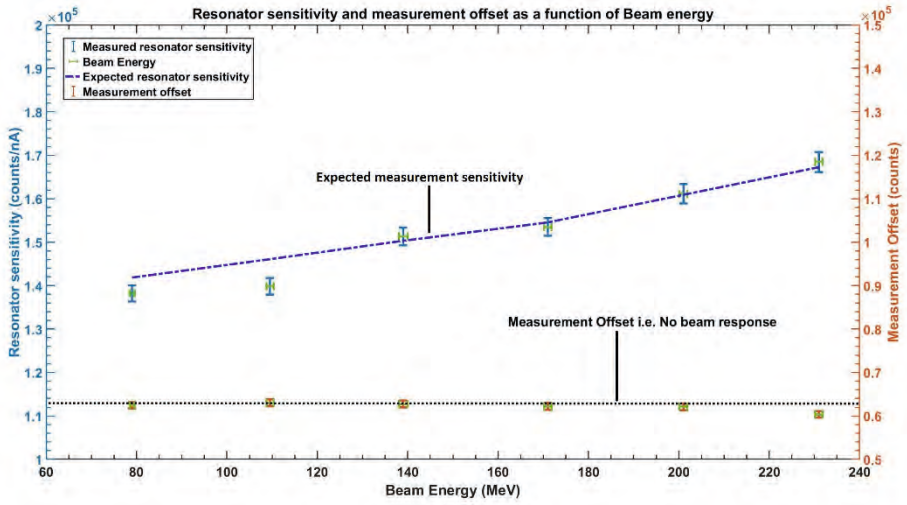

Figure 3.12: Resonator sensitivity and measurement offset dependence on beam energy. The resonator sensitivity decreases with energy due to the energy-dependent beam current. The data points are represented with one sigma deviation. Marked as dotted lines are the trend of the expected resonator sensitivity (blue) and the measurement offset agreement with no-beam resonator response (black).

The expected sensitivity, k, calculated from the expected relative dependence of the sensitivity as a function of energy, is within one sigma of the measured sensitivity, k_meas, for all energies except for 109 MeV (≈3 sigmas) and 79 MeV (≈2 sigmas). This could be due to higher correction applied for the signal losses in the IC due to its geometrical limitation (measurement window of the IC smaller than bunch width for lower energies). The product of the second harmonic amplitude factor, A_2, (from Table 3.2) with a normalizing term, C, provides the expected resonator sensitivity, k, in Table 3.4. The value of the normalizing term, C = 212042 counts/nA (C=161152/0.76), is derived by comparing the measured sensitivity, k_meas, with A_2 of 201 MeV.

Table 3.4 and Figure 3.12 show that the energy dependence of the resonator sensitivity is in reasonable agreement with our expectations. Thus, the linear-fit equations given in Figure 3.11 are used to determine the lowest detectable beam current.

We defined the lowest detectable beam current by the condition that the resonator response (i.e., I_{ResDDC}) is at least three sigmas (defined resolution) higher than the measurement offset. This condition provides the lowest detectable beam current as 0.15 nA with a resolution of 0.05 nA for all energies as derived from the fit equations given in Figure 3.11.

3.7 Discussion

The prototype cavity resonator has been validated as a beam current monitor both in the test-bench environment and in the beamline. The test-bench characterization of the cavity without the stretched wire helped to identify a difference of approximately 5% in the dielectric constant of macor. A new macor ring with the final optimal width 33 mm and thickness of 12.42 mm has been installed in the prototype before estimating the beam-to-pickup sensitivity in the test-bench. A good agreement of the signal estimate and the loaded quality factor with respect to simulation results was found. The position dependency of the cavity resonator is only 0.03%/mm up to a distance corresponding to 60% of the beam pipe radius. Compared to Fast Current Transformers, whose position dependency is greater than 1%/mm [23], we conclude that cavity resonators are better suited for position independent beam current measurements.

The energy dependence of the resonator sensitivity is in reasonable agreement with our expectations and indicates that a calibration of the cavity resonator

should be made for different energies and momentum slit apertures in the ESS at each location where it is installed.

Especially for energies 109 MeV and 79 MeV, the higher deviation between the expected and the measured sensitivity calls for an accurate correction for the signal losses (in the IC due to geometrical limitations). In other words, an absolute measure of the beam current and momentum spread is necessary to have a good calibration of the resonator, which would provide a good agreement of the sensitivity within one sigma with respect to the expected trend of the sensitivity. Although most treatments are done with the same maximum momentum spread (set by ESS slit aperture), the dependence of the sensitivity on the actual momentum spread should also be calibrated.

It is also important to remember that the measured sensitivity is valid only for the present location of the resonator, i.e., 16 meters from the degrader. Any relocation of the resonator requires a new calibration for each individual energy and the transmitted momentum spread. The need to calibrate individually at multiple energies can be replaced by single energy calibration with the relocation of the resonator at the immediate proximity of the degrader exit. This is because the bunch length elongation due to the beam energy spread induced by the degrader is then smaller and for more downstream located cavity resonators, the energy dependence is then only determined by the (fixed) distance to the degrader.

The calibration performed should be considered invariant with time since PROSCAN is a temperature-controlled environment. Thus, reliable beam currents can be measured with the sensitivity derived from the measurements.

The good agreement between the no-beam resonator response and the measurement offset from the in-beam measurements suggests that the cavity response and the measurement offset are uncorrelated.

Although beam currents down to 0.15 nA can be measured with 0.05 nA resolution with the existing setup, measurement of beam currents down to 0.1 nA could be achieved. This is possible with an ideal RF isolation of the cavity, which can lower the measurement offset to 40000 counts. This also improves the sensitivity by a factor of 1.5 approximately and an improved signal resolution of 0.03 nA.

Further performance improvements of this resonator are possible with the design of the resonator as a single port or with improved impedance matching (with matching circuits) at the measurement port in the multiport resonator. Both

methods are expected to improve the signal level by up to 50% for a given beam current.

The cavity resonator can provide beam current information for the range 0.1-10 nA with 0.05 nA resolution using an integration time of 1 second. This limits the functionality of the resonator in patient treatments. The cavity resonator can be used for optimizing the beam transport properties as well as in controlling the operation parameters within the normal ranges.

In circumstances such as daily quality checks and high beam current irradiation, as in FLASH (very high dose rate) experiments, a cavity resonator is advantageous and could replace ICs. Especially, FLASH experiments could pose a risk for ICs due to the space charge effect that could result in a non-linear response. The use of the cavity resonator will relay all the necessary measures [24], required for the proper functioning of the ICs. Moreover, if proton FLASH therapy becomes available for clinical treatment in the future (possible only for high energies with existing accelerators), a cavity resonator could be used during patient treatment since the beam currents are in the range of hundreds of nA [25]. This would lower the integration time to a few tens of microseconds enabling real-time beam monitoring and feedback to the control system.

3.8 Conclusion

In this work, we have demonstrated successful non-invasive beam current measurements at a proton therapy facility in the range 0.1-10 nA for the energy range 231-79 MeV. This relative beam current measurement has been achieved with a resolution of 0.05 nA with the help of a dielectric-filled reentrant cavity resonator. To our knowledge, this is the first time, non-invasive beam current measurement has been achieved at a proton therapy facility. These results indicate that cavity resonators have the potential to replace several of the ICs for beam current measurements at proton therapy facilities.

3.9 Appendix

FCL100 Linear Drive

3TA 1: Mechanical specifications and load characteristics of the FCL100 series linear drive

Specifications	FCL100
Travel Range (mm)	100
Minimum incremental motion (µm)	0.15
Bi-directional repeatability (µm)	5
On-axis accuracy (µm)	5
Pitch (µrad)	100
Yaw (µrad)	100
Axial load capacity (N)	40
Weight (kg)	3.6

ZNB8 Vector Network Analyzer

The vector network analyzer is with a source impedance of 50 Ω and with 4 test ports. The frequency range of operation is from 9 kHz to 8.5 GHz. In a transmission measurement, the analyzer transmits a stimulus signal to the input port of the Device Under Test (DUT) and measures the transmitted wave at the DUT's output port. Before any measurement, it is recommended to preset the instrument to establish a well-defined instrument state. Prior to any measurement, it is also important to calibrate the test-bench measurement setup, as we can eliminate systematic, reproducible errors from cables and setup. The TSOM (Through, Short, Open, and Match) calibration with the help of the provided calibration kit has been used to minimize the systematic measurement errors.

3.10 References

[1] Newport, “FCL Series Linear Stages User ’ s Manual.” 2019.

[2] Rohde & Schwarz GmbH & Co. KG., “R & S ZNB / ZNBT Vector Network Analyzers User Manual,” vol. 15, 2014.

[3] Rohde & Schwarz, “ZNB Vector Network Analyzer Specifications,” 2017. ZNB_dat-sw_en_5214-5384-22_v0900_96dp.pdf (accessed Mar. 09, 2020).

[4] R. C. Authors *et al.*, “Autodesk Inventor,” no. September 2007, 2008.

[5] Agilent Technologies, “Understanding the Fundamental Principles of Vector Network Analysis,” *Appl. Note 5965-7707E*, p. 15, 2012, [Online]. Available: http://www.agilent.com/.

[6] “Macor,” *Corning Inc. Light. Mater.*, 2009, [Online]. Available: http://psec.uchicago.edu/ceramics/MACOR Data Sheet.pdf.

[7] D. Lipka, “Cavity Bpm Designs , Related Electronics and Measured Performances,” in *Proceedings of DIPAC09*, 2009, pp. 280–284, [Online]. Available: dipac09.web.psi.ch.

[8] V. Rizzoglio *et al.*, “Evolution of a beam dynamics model for the transport line in a proton therapy facility,” *Phys. Rev. Accel. Beams*, vol. 20, no. 12, pp. 1–12, 2017, doi: 10.1103/PhysRevAccelBeams.20.124702.

[9] F. J. M. Farley, “Optimum strategy for energy degraders and ionization cooling,” *Nucl. Instruments Methods Phys. Res. Sect. A Accel. Spectrometers, Detect. Assoc. Equip.*, vol. 540, no. 2–3, pp. 235–244, 2005, doi: 10.1016/j.nima.2004.11.034.

[10] V. Anferov, “Energy degrader optimization for medical beam lines,” *Nucl. Instruments Methods Phys. Res. Sect. A Accel. Spectrometers, Detect. Assoc. Equip.*, vol. 496, no. 1, pp. 222–227, 2003, doi: 10.1016/S0168-9002(02)01625-X.

[11] J. Petzoldt *et al.*, “Characterization of the microbunch time structure of proton pencil beams at a clinical treatment facility,” *Phys. Med. Biol.*, vol. 61, no. 6, pp. 2432–2456, 2016, doi: 10.1088/0031-9155/61/6/2432.

[12] P. Vavilov, “Ionization Losses of High-Energy Heavy Particles,” *Sov. Phys. JETP*, vol. Vol: 5, no. 4, pp. 749–751, 1957.

[13] M. J. Van Goethem, R. Van Der Meer, H. W. Reist, and J. M. Schippers, “Geant4 simulations of proton beam transport through a carbon or

beryllium degrader and following a beam line," *Phys. Med. Biol.*, vol. 54, no. 19, pp. 5831–5846, 2009, doi: 10.1088/0031-9155/54/19/011.

[14] R. E. Shafer, "Beam Position Monitoring," *AIP Conf. Proc.*, vol. 212, pp. 26–58, 1990, doi: 10.1063/1.39710.

[15] E. Johansen, "VME MESTRA Rev C Specification," 2020. doi: 10.5281/zenodo.3887550.

[16] "R&K-LA120-0S LOW NOISE AMPLIFIER." http://www.rk-microwave.com/jp/products/pdf/LA120-0S_01.pdf (accessed Jan. 16, 2020).

[17] "K&L Microwave." http://www.klmicrowave.com/ (accessed Feb. 01, 2020).

[18] FEMTO, "Datasheet Ultra-Wideband Voltage Amplifier DUPVA-1-70 Variable-Gain." www.femto.de (accessed Jan. 15, 2020).

[19] Mini-circuits, "Low Noise Amplifier - S-Band." https://www.minicircuits.com/pdfs/ZX60-P103LN+.pdf (accessed Jan. 16, 2020).

[20] "ADC _ 3110 / 3111 – Eight Channel 16-bit ADC Data Sheet." https://www.ioxos.ch/produit/adc-3110-3111/ (accessed Jan. 15, 2020).

[21] R. Dölling, "Profile, Current, and Halo Monitors of the PROSCAN Beam Lines," in *AIP Conference Proceedings*, 2004, vol. 732, pp. 244–252, doi: 10.1063/1.1831154.

[22] P. A. Duperrex, "Latest Diagnostic Electronics Development for the PROSCAN Proton Accelerator," *AIP Conf. Proc.*, vol. 732, pp. 268–275, 2004, doi: 10.1063/1.1831157.

[23] P. Odier, D. Belohrad, J.-J. Gras, and M. Ludwig, "Operational experience and improvements of the LHC beam current transformers," in *Proceedings of the 10th European Workshop on Beam diagnostics and Instrumentation for Particle Accelerators*, 2011.

[24] R. Dölling, "Ionization chambers and secondary emission monitors at the PROSCAN beam lines," *AIP Conf. Proc.*, vol. 868, pp. 271–280, 2006, doi: 10.1063/1.2401414.

[25] A. Patriarca *et al.*, "Experimental Set-up for FLASH Proton Irradiation of Small Animals Using a Clinical System," *Int. J. Radiat. Oncol. Biol. Phys.*, 2018, doi: 10.1016/j.ijrobp.2018.06.403.